Structure–Activity Relationship in Manganese Perovskite Oxide Nanocrystals from Molten Salts for Efficient Oxygen Reduction Reaction Electrocatalysis

Francisco Gonell, Carlos M Sánchez-Sánchez, Vincent Vivier, Christophe Méthivier, Christel Laberty-Robert, David Portehault

Structure-activity relationship in manganese perovskite oxide nanocrystals from molten salts for efficient oxygen reduction reaction electrocatalysis

Francisco Gonell,[a] Carlos M. Sánchez-Sánchez,[b] Vincent Vivier,[b] Christophe Méthivier,[c] Christel Laberty-Robert,[a] David Portehault*[a]

[a] Sorbonne Université, CNRS, Collège de France, Laboratoire de Chimie de la Matière Condensée de Paris (CMCP), 4 place Jussieu, F-75005, Paris, France

[b] Sorbonne Université, CNRS, Laboratoire Interfaces et Systèmes Electrochimiques (LISE), 4 place Jussieu, F-75005, Paris, France

[c] Sorbonne Université, CNRS, Laboratoire de Réactivité de la Surface (LRS), 4 place Jussieu, F-75005, Paris, France

ABSTRACT: We report a synthesis pathway in molten salts toward ligand-free nanoparticles of the layered perovskite $La_{0.5}Sr_{1.5}MnO_4$ (l-LSMO) and of the pseudo-cubic perovskite $La_{0.7}Sr_{0.3}MnO_3$ (pc-LSMO). These particles are readily implemented as oxygen reduction reaction (ORR) electrocatalysts in alkaline conditions. They show high ORR selectivity for the 4-electrons reduction of O2 in water. Among these two materials, pc-LSMO nanocrystals of 20 nm diameter exhibit high mass-normalized ORR activity for a perovskite material (21.4 A g^{-1}_{oxide} at 0.8 V/RHE) thanks to their relatively large surface area, high crystallinity and electron mobility. These features provide pc-LSMO nanocrystals with remarkable stability compared to state-of-the-art perovskites, for instance only a 5% increase of the overpotential at -0.05 mA cm^{-2}_{oxide} over 40 hours. pc-LSMO nanocrystals are then the most stable perovskite ORR electrocatalyst reported up to now. These performances, combined with high activity, high selectivity and absence of precious metals, make $La_{0.7}Sr_{0.3}MnO_3$ nanocrystals one of the best compromises for alkaline oxygen reduction reaction.

Manganese-based oxides are promising precious metal-free electrocatalysts of the oxygen reduction reaction (ORR) for alkaline fuel cells.[1,2] Both Mn octahedral coordination and mixed valence Mn^{3+} / Mn^{4+} are critical parameters to provide high ORR electrocatalytic activity.[3–5] These requirements are met in pseudo-cubic perovskite manganites with general formula $AMnO_3$ and layered perovskite Ruddlesden-Popper (RP) manganites $A_{n+1}Mn_nO_{3n+1}$ (or $(AO)(AMnO_3)_n$ n = 1, 2...) that withstand numerous cationic substitutions, mixed Mn valences and lattice distortions.[3,6–11] RP manganites contain layers of n $AMnO_3$ perovskite units alternating with AO rock-salt layers, which provide additional anionic conductivity.[9,12,13] This feature should increase electrocatalytic activity.[14] Strategies explored to enhance the ORR electrocatalytic activity of manganese-based oxides focus on increasing the surface area of the materials in order to provide more active sites per mass unit compared to the large crystals typically obtained with solid-state synthesis. This goal has been pursued either by decreasing particle size[15] or by designing macroporous perovskites[16] by using sol-gel-based synthesis related to the Pechini process.[17] These approaches require a final treatment at high temperature in order to crystallize the perovskite structure. This treatment delivers manganites with relatively low surface area[16], highly aggregated particles, ill-defined morphology, and large density of crystal defects,[18] which hinder charge transfer, ORR electrocatalysis and overall control of catalytic properties.[3] The low surface area bottleneck has been recently overcome by using nanoparticles as reagents during sol-gel-based syntheses, yielding high mass-normalized activity.[19] Designing manganese perovskites nanomaterials with small particle size but also high crystallinity should further enhance stability during electrocatalysis, but this level of materials design could not been reached through sol-gel-based processes.

In the present work we aim at synthesizing, studying and comparing the ORR electrocatalytic properties of nanoscaled pseudo-cubic and layered perovskite manganites in order to (i) report the ORR electrocatalytic properties of RP manganites at room temperature in alkaline aqueous medium , (ii) study the role of the dimensionality of perovskite-related crystal structures in ORR electrocatalysis; (iii) highlight pseudo-cubic perovskite manga-

nite nanocrystals as high performance ORR electrocatalysts.

We draw on a one-step colloidal synthesis in inorganic molten salts. These liquids are stable at high temperatures and are then compatible with direct crystallization of the perovskites. In liquids, the nucleation rate is higher than in the above-mentioned methods, resulting in a decrease of the particle size. The manganite perovskite particles we report exhibit small sizes and organic ligand-free surfaces that are beneficial for charge transfer at the electrocatalyst interfaces, hence for electron percolation in the electrode, and for adsorption of dioxygen reagent. They also exhibit low amounts of crystal defects, again beneficial for charge transport[20,21] compared to sol-gel derived materials. Hence, the approach delivers highly active and stable manganite perovskite ORR electrocatalysts. In addition to the pseudo-cubic manganite $La_{0.7}Sr_{0.3}MnO_3$,[20,21] we synthesize the first layered manganite $La_{0.5}Sr_{1.5}MnO_4$ RP nanoparticles by tuning the oxo-basicity of the molten medium. We report for the first time the mechanisms of nanoparticles formation in high temperature molten salts and highlight the key experimental parameters enabling structural control. We show high mass-normalized ORR activity for perovskites. Highly crystalline $La_{0.7}Sr_{0.3}MnO_3$ nanocrystals also show remarkable stability of the ORR performances over 40 hours of operation, thus out-performing previously reported perovskites. These precious metal-free nanomaterials are a step forward for low-cost alternatives to precious metal-based electrocatalysts.

RESULTS AND DISCUSSION

Pseudo-cubic $La_{0.7}Sr_{0.3}MnO_3$ (pc-LSMO) nanocubes of 20 nm (**Figure 1a-b** and **Figure S1**) were produced according to a protocol we previously reported, using molten KNO_3 as a liquid medium at 600 °C where metal nitrates are decomposed.[21] When the reagents ratio was adjusted to target the layered perovskite $La_{0.5}Sr_{1.5}MnO_4$ (l-LSMO) in the same conditions, the reaction yielded only the pseudo-cubic structure (**Figure S2**). Increasing the Sr/Mn ratio and the temperature up to 800 °C (**Table S1**) triggered crystallization of the layered structure (**Figure S2**), but the cationic content evaluated by wavelength dispersive X-ray fluorescence (WDXRF, **Table S1**) showed that all La^{3+} and Sr^{2+} cations were not incorporated in the solid, as suggested by $La(OH)_3$ and $SrCO_3$ impurities identified by X-ray diffraction (XRD, **Figure S2**). To trigger full incorporation of the remaining cations, the oxo-basicity of the solvent was increased by using molten $NaNO_2$ instead of KNO_3.[22,23] Although the pseudo-cubic structure was again obtained at 600 °C (**Figure 1i** and **Figure S3**), the reaction was completed at 800 °C and yielded l-LSMO as the only crystalline phase with composition $La_{0.5}Sr_{1.5}MnO_4$ according to WDXRF (**Table S1**). The l-LSMO Scherrer crystal size of 67 nm is smaller than reported values for RP manganite particles.[24–28] SEM and TEM (**Figure 1c-g,** respectively) show that the l-LSMO sample is made of cube-like particles with a broad size distribution between 50-200 nm in agreement with the crystallite size. Selected area electron diffraction (SAED, **Figure 1e inset**) and the Fast Fourier Transform-analyzed HRTEM (**Figure 1h**) show spot-like patterns indicating well-oriented crystallites within the same particle. Nitrogen sorption yields a BET surface area of 8 $m^2 g^{-1}$, smaller than the 36 $m^2 g^{-1}$ measured for pc-LSMO, in agreement with the larger particle size of l-LSMO.

pc-LSMO (**Figure 1i**) is a reaction intermediate at 600 °C that evolves to the layered phase at 800 °C. This was confirmed by redispersing into $NaNO_2$ pre-synthesized pc-

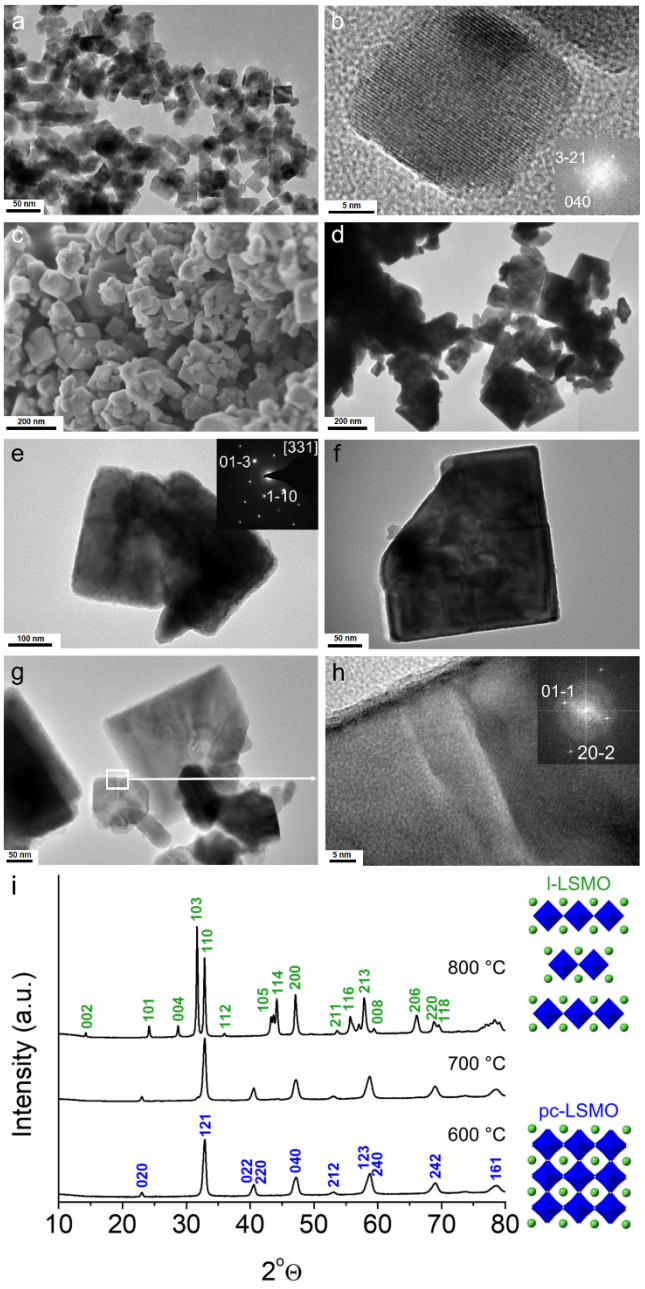

Figure 1. (a) TEM and (b) HRTEM images of pc-LSMO nanocubes. (c) SEM and (d-g) TEM images of l-LSMO nano-

particles (SAED pattern as inset in (e) indexed along the [331] zone axis). (h) HRTEM image of a l-LSMO nanoparticle and corresponding Fast Fourier Transform. (i) XRD patterns (Cu K_α) of the powders obtained by targeting l-LSMO in molten $NaNO_2$ at several reaction temperatures for 15 minutes.

LSMO nanoparticles (**Figure 1a-b** and **Figure S1**) with additional amounts of $Sr(NO_3)_2$ meeting the stoichiometry of the layered phase. The XRD patterns of the powders recovered after heating (**Figure S4**) show a phase evolution towards l-LSMO with a temperature increase, similar to the direct syntheses from the salts described above. A blank treatment of pc-LSMO nanocubes into molten $NaNO_2$ at 800 °C without additional Sr^{2+} source yielded crystalline $La(OH)_3$ (**Figure S5**) and amorphous matter after water washing. This suggests that before exposure to water, the reaction medium actually contained dissolved La^{3+} ions. Thus, pc-LSMO was solubilized in molten $NaNO_2$. The dissolution of pc-LSMO in this blank treatment indicates that the l-LSMO on-pot synthesis proceeds through pc-LSMO dissolution followed by l-LSMO recrystallization (**Figure 2**).

The ORR activity in alkaline solution of l-LSMO and pc-LSMO nanomaterials was evaluated on catalyst/Nafion/carbon black composite electrode films deposited on a glassy carbon rotating disk substrate. The cyclic voltammograms (CVs) in 0.1 m KOH were first normalized to the area of the glassy carbon collector, corresponding to a constant catalyst mass loading (0.136 mg cm^{-2}, **Figure 3a**). The cathodic current density at

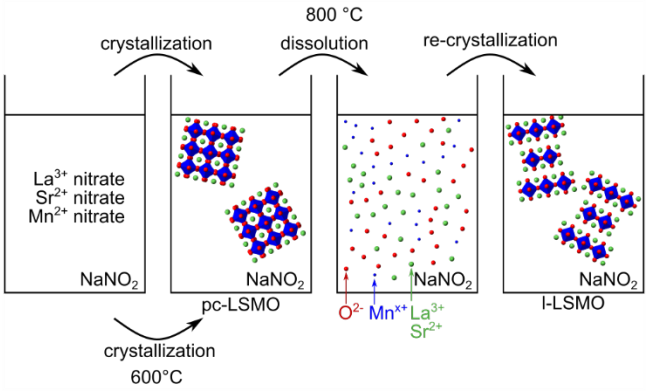

Figure 2. Reaction pathway yielding layered perovskite (l-LSMO) nanoparticles from pc-LSMO into molten $NaNO_2$.

0.4 V/RHE for pc-LSMO is almost twice that of l-LSMO. pc-LSMO nanocrystals show high mass-normalized ORR activity for oxide perovskites (21.4 A g^{-1}_{oxide} at 0.8 V/RHE, **Table S2**)[4,5,14–16,29,30] thanks to the combination of their high crystallinity and relatively large surface area. The disk surface-normalized activity of pc-LSMO nanocrystals is close to the benchmark precious metal catalyst (Pt/C) (**Figure S6**). For comparison of the specific activities, the current density was normalized *versus* BET surface areas (**Figure 3b**). At 0.4 V/RHE, l-LSMO exhibits a cathodic specific current density of ca. -1 mA cm^{-2}_{oxide}, twice larger than pc-LSMO. At a lower specific current density of -40 μA cm^{-2}_{oxide}, pc-LSMO and l-LSMO operate at 0.86 and 0.83 V/RHE, respectively (**Figure 3b** inset), thus indicating that the cubic phase is the most active at low overpotentials. This is corroborated by Tafel slopes (**Figure S7**) of 56 and 99 mV dec^{-1} for pc-LSMO and l-LSMO, respectively, in good agreement with previous works.[3,5] Both materials exhibit surface-normalized electrocatalytic activities (0.85 V vs RHE for 40 μA cm^{-2}_{oxide}) matching those of most active

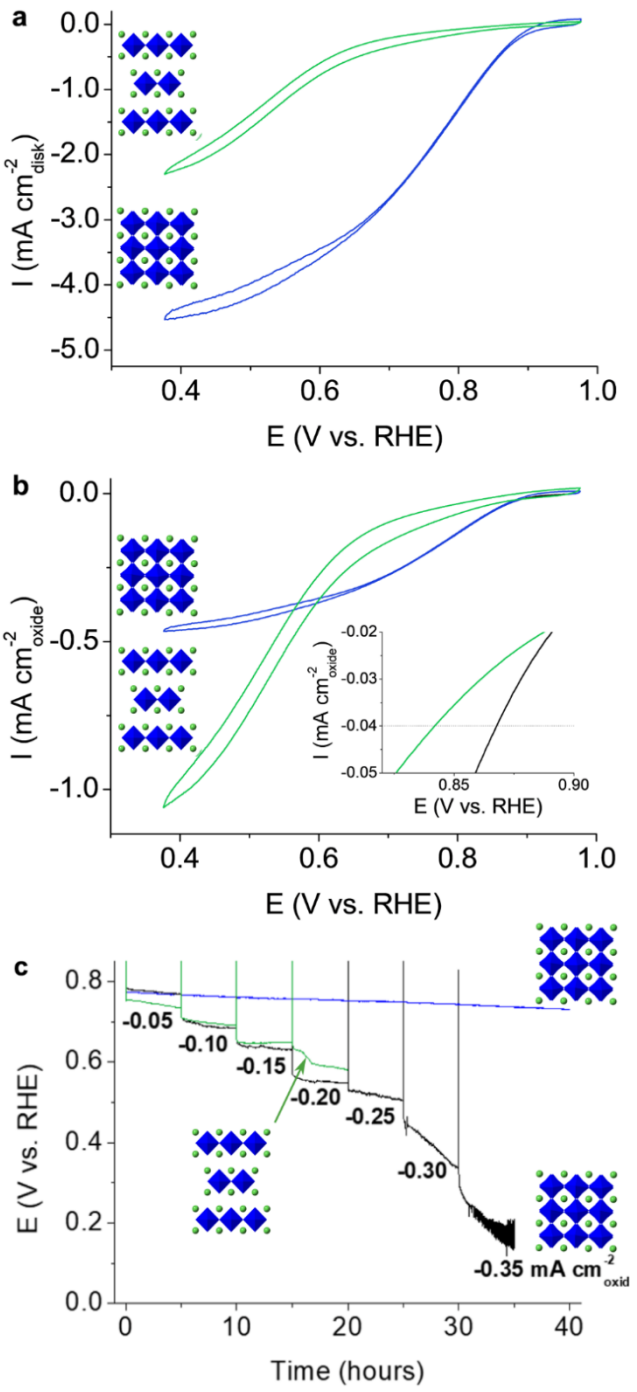

Figure 3. ORR electrocatalytic activity of pseudo-cubic pc-LSMO (blue curves) and layered l-LSMO (green curves) Mn perovskites (O_2-saturated 0.1 m KOH electrolyte, 10 mV s^{-1}

and 1600 rpm). (a) Electrode area-normalized and (b) BET surface-normalized cyclic voltammograms. (c) Chronopotentiometry curves of pc-LSMO at -0.05 mA cm^{-2}_{oxide} (blue) and of pc-LSMO (black) and l-LSMO (green) at several current densities.

manganese perovskite epitaxial thin films grown by pulsed laser deposition.[3] This demonstrates the high crystalline quality of the nanocrystals produced in molten salts, which provides high electronic conduction. The synthesis in molten salts differs from conventional colloidal synthesis in organic solvents, as it delivers materials with surfaces free of any insulating organic ligands. These ligand-free surfaces also contribute to enhanced charge percolation and electrocatalytic activity.

The number of electrons transferred during ORR is between 3.9 and 4.0 according to a Koutecky-Levich analysis of the diffusion current at 0.4 V/RHE (**Figure S8**), in very good agreement with the theoretical 4-electrons value for the overall reduction reaction of O_2 into H_2O (**Figure S9** left).[4,5] This was also confirmed by scanning electrochemical microscopy experiments (SECM) that could not detect any corrosive HO_2^- byproduct during ORR for both electrocatalysts in the whole potential range (**Figure S10**). In addition, the acetylene black (AB) carbon additive shows a negligible activity above 0.6 V vs RHE and a low activity at lower potential (**Figure S6**). This further confirms that the perovskites are the only active materials above 0.6 V vs RHE. The absence of any HO_2^- byproduct detected in the vicinity of the electrode by SECM also enables to rule out possible activity of the acetylene black additive through formation of an H2O2 intermediate: the reaction proceeds only through a 4-electrons reduction pathway at the surface of the perovskite catalysts. This makes these manganese-based perovskites ideal for implementation into fuel cells. The reaction mechanism was further confirmed by probing the effect of surface hydroxylation and hydrophobicity on the overall ORR disk area-normalized current density (see details in **Figure S11-S15** and **Table S3**), as previously described for OER electrocatalysts.[31,32]

The ratio between Mn^{3+} and Mn^{4+} plays a crucial role in the ORR kinetics. According to a model describing localized orbitals on surface Mn cations,[3,5] the optimum AOS for ORR is expected at 3.3 for pseudo-cubic manganite perovskites, where the best compromise is reached between O_2^-/OH^- exchange at the surface of the catalyst, and the regeneration of OH^-. In the present case, chemical titration yields average Mn oxidation states (AOS) of 3.6 and 3.3 in pc-LSMO and l-LSMO, respectively. Hence, l-LSMO would be expected as the most active electrocatalyst, which disagrees with our observations at low overpotential. This apparent discrepancy may originate first from a change in the oxidation state of Mn at the surface of the particles. Indeed, we have previously shown that Mn is reduced within a 1 nm-thick layer at the surface of pc-LSMO nanocubes because of oxygen vacancies,[21,33] yielding a surface Mn oxidation state close to 3.3.[33] Likewise, X-ray photoelectron spectroscopy (XPS, **Figure S16**) yields a surface Mn oxidation state of 3.2 for l-LSMO. Given the precision of XPS (±0.1 on the oxidation state), pc-LSMO and l-LSMO possess identical surface oxidation states. Hence, both the pseudo-cubic and the layered perovskite samples exhibit at their surface the Mn oxidation state optimal for ORR, which rules out surface oxidation states as a possible origin for the higher activity of pc-LSMO. Therefore, the difference in ORR activity between both materials presumably relates to charge-transfer kinetics within the whole materials (**Figure S9** right). At room temperature with the measured average AOS, the pseudo-cubic phase is metallic whereas the layered phase is semi-conducting.[34] Then, electronic conduction is larger in pc-LSMO and enhances electrocatalytic activity at low overpotential.[3] On the opposite, at high overpotential, below 0.6 V/RHE, we observe a higher ORR current for l-LSMO compared to pc-LSMO. In these conditions, the conduction band of l-LSMO becomes populated and electronic conductivity is not limiting anymore the electrocatalytic process. The higher activity of l-LSMO may be related to the high ionic conductivity of the layered phase.

Finally, we have addressed the long-term stability of pc-LSMO and l-LSMO during ORR operation conditions by using chronopotentiometry (**Figure 3c**). pc-LSMO exhibits its remarkable stability at - 0.05 mA cm^{-2}_{oxide} with only a slight decrease of 5 %in the voltage (from 0.77 to 0.73 V/RHE) over 40 hours. pc-LSMO appears as the most stable ORR perovskite electrocatalyst reported up to now (**Table S2**). By successively increasing the cathodic current every 5 hours, pc-LSMO shows stable performances up to -0.30 mA cm^{-2}_{oxide} where the electrocatalytic activity drastically decreases. The electrocatalytic activity of l-LSMO is less stable and drops at -0.20 mA cm^{-2}_{oxide}. These results are confirmed by the CVs measured before and after each current step applied in chronopotentiometry where a decrease of the cathodic current is observed (**Figure S17**).

In order to gain insights into the deactivation process, the materials were recovered after chonopotentiometry and studied by HRTEM and STEM-EDS. After operation during 40 h at -0.05 mA cm^{-2}_{oxide}, pc-LSMO exhibits the same well faceted cubic morphology as the fresh material, with particles still crystallized into the pc-LSMO structure (**Figure 4a-c**). The same material observed after successively increasing the cathodic current up to -0.35 mA cm^{-2}_{oxide} and 35 h still shows well faceted particles, but others have lost their morphology and got amorphized (**Figure 4d-f**). l-LSMO shows more severe damage, as up to a current density of -0.20 mA cm^{-2}_{oxide} and after 20 h of operation, a 3-4 nm-thick amorphous layer appeared at the sur face of the particles (**Figure 3g-i**). EDS analysis of electrode material performed in a scanning electron microscope (SEM) indicates that the cationic composition did not change significantly (**Table S4**). STEM-EDS mapping of the post-mortem electrode also shows homogeneous element distribution (**Figure S18-S20**). Hence, the deactivation during ORR is related to surface amorphization. This phenomenon is more extended for the layered perovskite, which may be ascribed to its layered structure

that provides larger ion conduction[13] and then extended reaction with the electrolyte. On the contrary, pc-LSMO shows very high stability compared to other Mn-based materials already reported (**Table S2**). ORR has been previously evaluated only on Mn perovskite nanoparticles produced by sol-gel-derived methods, which yield large amounts of crystal defects.[15,16] Herein we demonstrate that the higher

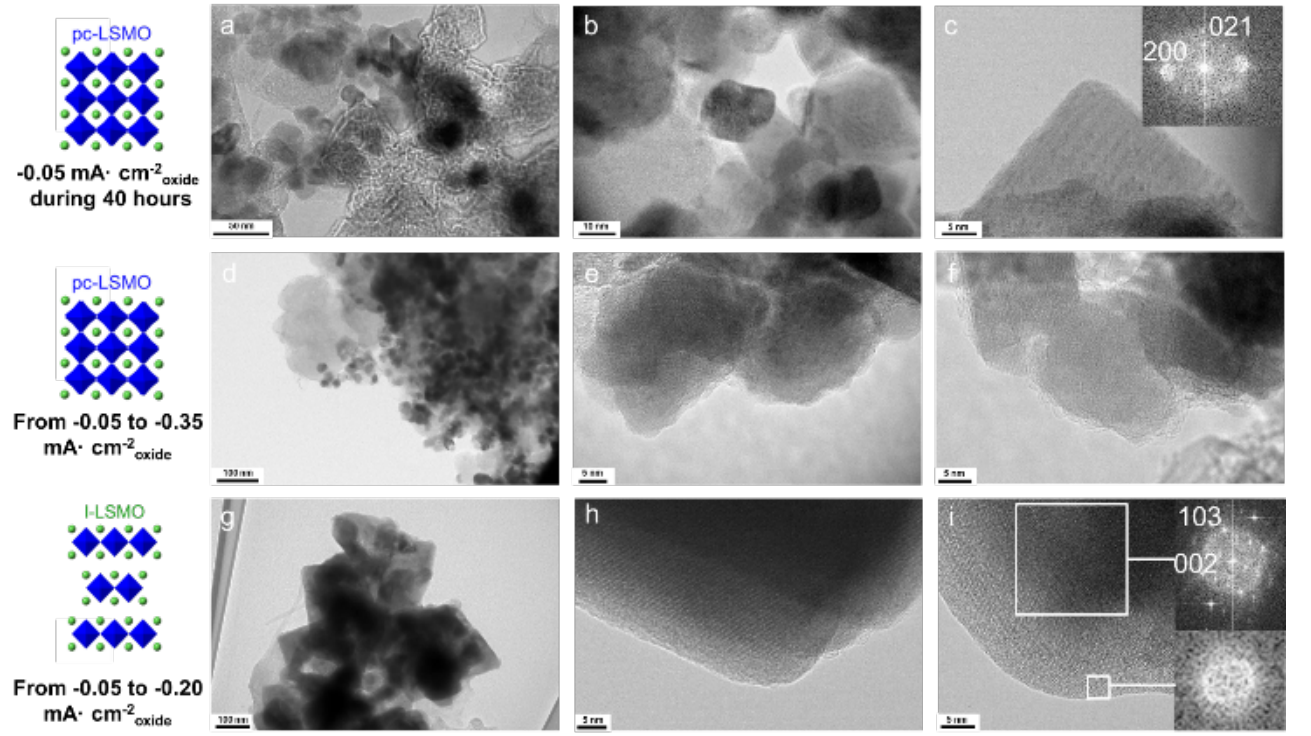

Figure 4. TEM and HRTEM micrographs of pc-LSMO after chronopotentiometry in 0.1 m KOH at (a-c) -0.05 mA cm^{-2}_{oxide} during 40 hours and (d-f) after increasing current densities (from -0.05 to -0.35 mA cm^{-2}_{oxide}, see Figure 2c). (g-i) TEM and HRTEM micrographs of l-LSMO after increasing current densities (from -0.05 to -0.20 mA cm^{-2}_{oxide}, see Figure 2c). The Fast Fourier Transforms in (i) show that the material is crystallized in the particle core but amorphous in a 3-4 nm-thick layer.

crystallinity of the molten salts-derived nanocrystals ensures higher long-term stability under ORR operation conditions of those materials and of their electrochemical activity

CONCLUSIONS

Herein we have reported the synthesis of the layered $La_{0.5}Sr_{1.5}MnO_4$ perovskite (l-LMSO) in the nanoscale range for the first time. Accurate control of the solvent composition and thermal treatment allows obtaining pure pc-LSMO and l-LSMO perovskites by deciphering the l-LSMO crystallization process through the dissolution of a pseudo-cubic perovskite followed by reprecipitation of the layered phase in the molten salts. The pseudo-cubic $La_{0.7}Sr_{0.3}MnO_3$ (pc-LSMO) and layered $La_{0.5}Sr_{1.5}MnO_4$ perovskites exhibit high electrocatalytic activity for the ORR with high selectivity for the four-electrons O_2 reduction thanks to an optimized Mn oxidation state in the first surface atomic layers. l-LSMO shows high intrinsic (surface-normalized) electrocatalytic activity, despite its limited electronic conductivity *versus* the pseudo-cubic phase. However, the layered structure is poorly stable in operation conditions, probably due to its high ionic conductivity. On the other hand, the pseudo-cubic perovskite exhibits small particle size with low amounts of crystal defects and no insulating organic ligands. These features ensure high electronic conductivity within the electrode, high activity and remarkable stability under ORR operation for $La_{0.7}Sr_{0.3}MnO_3$ nanocrystals, making pseudo-cubic manganite nanocrystals a promising precious metal-free electrocatalyst for alkaline fuel cells.

EXPERIMENTAL PROCEDURES

Synthesis

All reagents used in the synthesis were purchased from Aldrich, otherwise said, and used as received without further purification. Water used for washing is MilliQ® water.

Pseudo-cubic $La_{0.7}Sr_{0.3}MnO_3$ (pc-LSMO) synthesis: pc-LSMO was synthesized according to a previous study.[21] Briefly, 6.5 mmol of $Mn(NO_3)_2{\cdot}4H_2O$, 3.9 mmol of $La(NO_3)_3{\cdot}6H_2O$, 2.0 mmol of $Sr(NO_3)_2$ and 65 mmol of KNO_3 were mixed with a few drops of ethanol and milled in a Retsch MM400 ball miller at 20 Hz for 2 min. The mixture was then dried under vacuum at 40 °C overnight. 2.5 g were introduced in an alumina crucible and treated at 600 °C for two hours in a preheated muffle oven in air atmosphere. Then, the reaction was quenched at room temperature by removing the crucible from the hot oven. The material was washed by centrifugation with deion-

ized water several times until the conductance of the supernatant reached the one of the water used for washing. The powder was dried under vacuum at room temperature overnight.

Layered $La_{0.5}Sr_{1.5}MnO_4$ (l-LSMO) synthesis: 6.5 mmol of $Mn(NO_3)_2{\cdot}4H_2O$, 3.1 mmol of $La(NO_3)_3{\cdot}6H_2O$, 8.0 mmol of $Sr(NO_3)_2$ and 65 mmol of KNO_3 or 95 mmol of $NaNO_2$ were mixed with a few drops of ethanol and milled in a Retsch MM400 ball miller. The mixture was then dried under vacuum at 40 °C overnight. 2.5 g were introduced in an alumina crucible and treated at 600-800 °C for 15 min in air atmosphere. Then, the reaction was quenched at room temperature by removing the crucible from the oven. The material was washed by centrifugation with deionized water several times until the conductance of the washing waters reached the same value as deionized water. The powder was dried under vacuum at room temperature overnight.

Reactivity test of pc-LSMO into molten $NaNO_2$: 0.25 g (1.1 mmol) of pc-LSMO was mixed with 2.5 g of $NaNO_2$ and milled in an agate mortar, then dried overnight at 40 °C under vacuum. This mixture was introduced in an alumina crucible and treated at 800 °C for 15 min under air atmosphere. The reaction was then quenched at room temperature, the powder was washed with deionized water and dried as explained above.

Reactivity test of pc-LSMO into molten $NaNO_2$ in the presence of Sr^{2+} ions: 0.25 g (1.1 mmol) of pc-LSMO, 1.48 mmol of $Sr(NO_3)_2$ and 2.5 g of $NaNO_2$ were mixed and milled in an agate mortar, then dried overnight at 40 °C under vacuum. This mixture was introduced in an alumina crucible and treated at 700-800 °C for several durations under air atmosphere. The reaction was then quenched at room temperature, the powder was washed with deionized water and dried as explained above.

Characterization

Materials characterization. Powder X-ray Diffraction (XRD) was performed on a Bruker D8 advance diffractometer equipped with a Cu Kα source. The crystalline phases were identified according to the reference PDF cards 04-014-7255 for pseudo-cubic $La_{0.7}Sr_{0.3}MnO_3$, 01-083-2034 for $La(OH)_3$, 01-084-1778 for $SrCO_3$ and 04-013-5773 for $La_{0.5}Sr_{1.5}MnO_4$. Transmission electron microscopy (TEM) was performed on a JEOL JEM2100Plus LaB_6 working at an accelerating voltage of 200 kV. Field-emission scanning electron microscopy (FE-SEM) was carried out on a Hitachi SU-70 microscope. Atomic composition given by wavelength dispersive X-ray fluorescence (WDXRF) was measured on a Bruker S8 Tiger spectrometer after pelletizing the powder. The perovskite catalyst surface area was calculated from the adsorption branch of the N_2 sorption isotherm according to the BET method at 77 K using an ASAP 2010 equipment. Prior to sorption measurements, the powders were degassed at 300 °C for 4 h. The Mn Average Oxidation State (AOS) was determined following a previously reported protocol.[35] Briefly, the powders were dissolved in acidic media and the manganese species were reduced by Fe^{2+} in excess. The excess Fe^{2+} ions were titrated with $Cr_2O_7^{2-}$. The total amount of Mn was determined by UV-visible spectrophotometry by oxidizing it into permanganate. With these two independent experiments, the determination of Mn^{III} and Mn^{IV} proportions was made possible.

Electrochemical characterization. The electrocatalytic properties of the materials were studied through a three-electrode setup in an electrochemical cell using a Pt wire as a counter electrode, a saturated Ag/AgCl reference electrode and a glassy carbon (GC) rotating disk electrode (RDE) as a working electrode, connected to a VPS Biologic potentiostat. All potentials are referred in the text to the reversible hydrogen electrode (RHE, $E_{RHE} = E_{Ag/AgCl(sat)} + 0.197 + 0.059pH$). The GC RDE (geometrical disk area (0.07 cm^2), Radiometer Analytical) was polished with diamond paste (1 µm, BAS inc.) followed by diamond paste (0.05 µm, BAS inc.) to reach mirror grade before each experiment. Then, the GC disk was coated with a conductive ink that contains the different perovskite catalysts. This ink was composed by the perovskite catalyst powder, hydrophilized Acetylene Black carbon (AB, Alfa Aesar) (99.9+ %, 75 $m^2\ g^{-1}$) and Nafion-117 (5 wt. % solution in aliphatic alcohols, Sigma-Aldrich). AB was hydrophilized by treating 0.5 g of AB in 50 mL of HNO_3 20% at 80 °C under stirring overnight, followed by centrifugation, washing with water and vacuum drying. 10 mg of the perovskite catalyst powder, 10 mg of the modified AB and 10 mL of absolute ethanol were mixed and sonicated for 2 hours. Then, 435 µL of ion-exchanged Nafion solution (5 wt. % in aliphatic alcohols, Aldrich) was added and the suspension was sonicated for 5 min.

10 µL (for cyclic voltammetry (CV)) or 2 µL (for the chronopotentiometry) of the ink (catalyst:acetylene black (AB) = 1:1) were deposited on the polished GC electrode and dried during 1 hour. Lower amounts of the ink were used for chronopotentiometry in order to facilitate the detection of catalysts deactivation. A 20%Pt/C commercial sample (Alfa Aesar) was used for benchmarking. The ink was prepared using 12.5 mg of the material and the same amounts of EtOH and Nafion-117 as described above. 1.5 µL of this ink was deposited on the GC electrode for performing the CV. Note that higher catalyst:AB ratio (5:1, 50 mg catalyst and 10 mg AB and deposition of 6 µL on GC)[4] resulted in high polarization (**Figure S6**) corresponding to slow kinetics of electron transfer. This is probably due to poor electron transport in the electrode and between the electrode material and the current collector. Indeed, the high amounts of interfaces due to the nanoscale of the catalyst particles decreases electron percolation. The catalyst:AB ratio 1:1 was chosen to bypass this issue.

The films were hydrated with 0.1 M KOH electrolyte during 30 min before the experiments. All cyclic voltammograms and chronopotentiometry curves were performed in O_2 saturated 0.1 M KOH solution (pH = 13.3) at a scan rate of 10 mV s^{-1} and rotation speed of 1600 rpm. Each experiment was repeated 3 times to test reproducibility. The pH-dependent study in KOH and trimethylammonium hydroxide (TMAOH) was performed in 0.1, 0.03, 0.005

and 0.001 M electrolytes (pH 13.3, 12.8, 12.0 and 11.2 respectively). The ionic strength was corrected with KNO_3 or trimethylammonium nitrate ($TMANO_3$) to a 0.1 M total concentration of K^+ or TMA^+. The ORR activity of perovskite catalysts was evaluated by comparing the specific activity current density (I ($mA\ cm^{-2}_{oxide}$)), being the current per perovskite oxide surface measured by BET, and the mass activity current density (I ($A\ g^{-1}_{oxide}$)), being the current per perovskite oxide mass. The ORR selectivity was evaluated by the Koutecky-Levich analysis from RDE measurements and by scanning electrochemical microscopy (SECM). SECM measurements were carried out at room temperature using the substrate generation-tip collection (SG/TC) mode[36–39] in a home-made SECM microscope. A four-electrode configuration was employed, with the following electrodes: the catalyst ink deposited on a glassy carbon disk substrate (5 mm in diameter) as the substrate generator electrode, a platinum ultramicroelectrode (25 µm in diameter) as the tip collector, a Pt wire as the counter electrode and a Saturated Calomel Electrode (SCE) as the reference electrode. A cyclic voltammogram at the substrate electrode was recorded in a still air-saturated 0.1 M KOH solution at 10 $mV\ s^{-1}$. Meanwhile the platinum tip collector biased at 0.4 V/SCE was positioned at 25 µm from the substrate inside its diffusion layer in order to detect the electroactive species (HO_2^-) generated during the ORR.

ASSOCIATED CONTENT

Supporting Information

The Supporting Information ia availabre free of charge via the Internet at http://pubs.acs.org." at DOI:xxxxxxxxxxxxxxx
Characterization of the materials and electrocatalytic results not shown in the manuscript.

AUTHOR INFORMATION

Corresponding Author

*E-mail: david.portehault@sorbonne-universite.fr

ACKNOWLEDGMENT

This work has been supported by the Region Ile-de-France in the framework of the Domaine d'Intérêt Majeur DIM Nano-K and by the French national agency for research (ANR) under the project SALTYSPIN ANR-17-CE09-0005. DP and FG also thank the Fondation Collège de France for support.

REFERENCES

(1) Takahashi, T.; Iwahara, H. Ionic Conduction in Perovskite-Type Oxide Solid Solution and Its Application to the Solid Electrolyte Fuel Cell. *Energy Convers.* **1971**, *11* (3), 105–111. https://doi.org/10.1016/0013-7480(71)90121-5.

(2) Miyazaki, K.; Sugimura, N.; Matsuoka, K.; Iriyama, Y.; Abe, T.; Matsuoka, M.; Ogumi, Z. Perovskite-Type Oxides La1–xSrxMnO3 for Cathode Catalysts in Direct Ethylene Glycol Alkaline Fuel Cells. *J. Power Sources* **2008**, *178* (2), 683–686. https://doi.org/10.1016/j.jpowsour.2007.08.007.

(3) Stoerzinger, K. A.; Lü, W.; Li, C.; Ariando; Venkatesan, T.; Shao-Horn, Y. Highly Active Epitaxial La (1– x) Sr x MnO 3 Surfaces for the Oxygen Reduction Reaction: Role of Charge Transfer. *J. Phys. Chem. Lett.* **2015**, *6* (8), 1435–1440. https://doi.org/10.1021/acs.jpclett.5b00439.

(4) Suntivich, J.; Gasteiger, H. A.; Yabuuchi, N.; Nakanishi, H.; Goodenough, J. B.; Shao-Horn, Y. Design Principles for Oxygen-Reduction Activity on Perovskite Oxide Catalysts for Fuel Cells and Metal–Air Batteries. *Nat. Chem.* **2011**, *3* (7), 546–550. https://doi.org/10.1038/nchem.1069.

(5) Stoerzinger, K. A.; Risch, M.; Han, B.; Shao-Horn, Y. Recent Insights into Manganese Oxides in Catalyzing Oxygen Reduction Kinetics. *ACS Catal.* **2015**, *5* (10), 6021–6031. https://doi.org/10.1021/acscatal.5b01444.

(6) Ansari, M. I. H.; Qurashi, A.; Nazeeruddin, M. K. Frontiers, Opportunities, and Challenges in Perovskite Solar Cells: A Critical Review. *J. Photochem. Photobiol. C Photochem. Rev.* **2018**, *35*, 1–24. https://doi.org/10.1016/j.jphotochemrev.2017.11.002.

(7) Hashim, S. S.; Somalu, M. R.; Loh, K. S.; Liu, S.; Zhou, W.; Sunarso, J. Perovskite-Based Proton Conducting Membranes for Hydrogen Separation: A Review. *Int. J. Hydrogen Energy* **2018**, *43* (32), 15281–15305. https://doi.org/10.1016/j.ijhydene.2018.06.045.

(8) Sunarso, J.; Hashim, S. S.; Zhu, N.; Zhou, W. Perovskite Oxides Applications in High Temperature Oxygen Separation, Solid Oxide Fuel Cell and Membrane Reactor: A Review. *Prog. Energy Combust. Sci.* **2017**, *61*, 57–77. https://doi.org/10.1016/j.pecs.2017.03.003.

(9) Ebrahimizadeh Abrishami, M.; Risch, M.; Scholz, J.; Roddatis, V.; Osterthun, N.; Jooss, C. Oxygen Evolution at Manganite Perovskite Ruddlesden-Popper Type Particles: Trends of Activity on Structure, Valence and Covalence. *Materials (Basel).* **2016**, *9* (11), 921. https://doi.org/10.3390/ma9110921.

(10) Battle, P. D.; Green, M. A.; Laskey, N. S.; Millburn, J. E.; Murphy, L.; Rosseinsky, M. J.; Sullivan, S. P.; Vente, J. F. Layered Ruddlesden–Popper Manganese Oxides: Synthesis and Cation Ordering. *Chem. Mater.* **1997**, *9* (2), 552–559. https://doi.org/10.1021/cm960398r.

(11) Sengodan, S.; Choi, S.; Jun, A.; Shin, T. H.; Ju, Y.-W.; Jeong, H. Y.; Shin, J.; Irvine, J. T. S.; Kim, G. Layered Oxygen-Deficient Double Perovskite as an Efficient and Stable Anode for Direct Hydrocarbon Solid Oxide Fuel Cells. *Nat. Mater.* **2015**, *14* (2), 205–209. https://doi.org/10.1038/nmat4166.

(12) Tarancón, A.; Burriel, M.; Santiso, J.; Skinner, S. J.; Kilner, J. A. Advances in Layered Oxide Cathodes for Intermediate Temperature Solid Oxide Fuel Cells. *J. Mater. Chem.* **2010**, *20* (19), 3799. https://doi.org/10.1039/b922430k.

(13) Lee, D.; Lee, H. Controlling Oxygen Mobility in Ruddlesden–Popper Oxides. *Materials (Basel).* **2017**, *10* (4), 368. https://doi.org/10.3390/ma10040368.

(14) Chen, D.; Wang, J.; Zhang, Z.; Shao, Z.; Ciucci, F. Boosting Oxygen Reduction/Evolution Reaction Activities with Layered Perovskite Catalysts. *Chem. Commun.* **2016**, *52* (71), 10739–10742. https://doi.org/10.1039/C6CC04895A.

(15) Du, J.; Zhang, T.; Cheng, F.; Chu, W.; Wu, Z.; Chen, J. Nonstoichiometric Perovskite CaMnO 3–δ for Oxygen Electrocatalysis with High Activity. *Inorg. Chem.* **2014**, *53* (17), 9106–9114. https://doi.org/10.1021/ic501631h.

(16) Lin, H.; Liu, P.; Wang, S.; Zhang, Z.; Dai, Z.; Tan, S.; Chen, D. A Highly Efficient Electrocatalyst for Oxygen Reduction Reaction: Three-Dimensionally Ordered Macroporous Perovskite LaMnO3. *J. Power Sources* **2019**, *412* (December 2018), 701–709. https://doi.org/10.1016/j.jpowsour.2018.12.005.

(17) M.P. Pechini. Method of Preparing Lead and Alkaline Earth Titanates and Niobates and Coating Method Using the Same to Form a Capacitor. No. 3,330,697, 1967.

(18) Epherre, R.; Duguet, E.; Mornet, S.; Pollert, E.; Louguet, S.; Lecommandoux, S.; Schatz, C.; Goglio, G. Manganite Perovskite Nanoparticles for Self-Controlled Magnetic Fluid Hyperthermia: About the Suitability of an Aqueous Combustion Synthesis Route. *J. Mater. Chem.* **2011**, *21* (12), 4393. https://doi.org/10.1039/cojm03963b.

(19) Cai, B.; Akkiraju, K.; Mounfield, W. P.; Wang, Z.; Li, X.; Huang, B.; Yuan, S.; Su, D.; Román-Leshkov, Y.; Shao-Horn, Y. Solid-State Gelation for Nanostructured Perovskite Oxide Aerogels. *Chem. Mater.* **2019**, 10.1021/acs.chemmater.9b03182. https://doi.org/10.1021/acs.chemmater.9b03182.

(20) Portehault, D.; Delacroix, S.; Gouget, G.; Grosjean, R.; Chan-Chang, T.-H.-C. Beyond the Compositional Threshold of Nanoparticle-Based Materials. *Acc. Chem. Res.* **2018**, *51* (4), 930–939. https://doi.org/10.1021/acs.accounts.7b00429.

(21) Thi N'Goc, H. Le; Mouafo, L. D. N.; Etrillard, C.; Torres-Pardo, A.; Dayen, J.-F.; Rano, S.; Rousse, G.; Laberty-Robert, C.; Calbet, J. G.; Drillon, M.; et al. Surface-Driven Magnetotransport in Perovskite Nanocrystals. *Adv. Mater.* **2017**, *29* (9), 1604745. https://doi.org/10.1002/adma.201604745.

(22) Al Raihani, H.; Durand, B.; Chassagneux, F.; Kerridge, D. H.; Inman, D. Zirconia Formation by Reaction of Zirconium Sulfate in Molten Alkali-Metal Nitrates or Nitrites. *J. Mater. Chem.* **1994**, *4* (8), 1331. https://doi.org/10.1039/jm9940401331.

(23) Houscroft, C. E.; Sharpe, A. G. *Inorganic Chemistry*, 2nd Ed.; Pearson Education Limited, 2005.

(24) Ehsani, M. H.; Mehrabad, M. J.; Kameli, P.; Ghazi, M. E.; Razavi, F. S. Low-Temperature Electrical Resistivity of Bilayered LaSr2Mn2O7 Manganite. *J. Low Temp. Phys.* **2016**, *183* (5–6), 359–370. https://doi.org/10.1007/s10909-016-1520-1.

(25) Ehsani, M. H.; Ghazi, M. E.; Kameli, P.; Razavi, F. S. DC Magnetization Studies of Nano- and Micro-Particles of Bilayered Manganite LaSr2Mn2O7. *J. Alloys Compd.* **2014**, *586*, 261–266. https://doi.org/10.1016/j.jallcom.2013.10.002.

(26) Ehsani, M. H.; Ghazi, M. E.; Kameli, P. Effects of PH and Sintering Temperature on the Synthesis and Electrical Properties of the Bilayered LaSr2Mn2O7 Manganite Prepared by the Sol–Gel Process. *J. Mater. Sci.* **2012**, *47* (15), 5815–5822. https://doi.org/10.1007/s10853-012-6481-4.

(27) Hue, D. T. M.; Manh, T. V; Anh, L. H.; Hong, L. V; Phan, M. H.; Huyen, P. T.; Chinh, H. D. Sol – Gel Synthesis , Characterization , and Magnetic Properties of Double-Layered Perovskite Manganite La1.25Sr1.75Mn2O7. *IEEE Trans. Magn.* **2014**, *50* (6), 2503204–2503204.

(28) Ehsani, M. H.; Kameli, P.; Ghazi, M. E. Influence of Grain Size on the Electrical Properties of the Double-Layered LaSr2Mn2O7 Manganite. *J. Phys. Chem. Solids* **2012**, *73* (6), 744–750. https://doi.org/10.1016/j.jpcs.2012.01.020.

(29) Celorrio, V.; Calvillo, L.; Dann, E.; Granozzi, G.; Aguadero, A.; Kramer, D.; Russell, A. E.; Fermín, D. J. Oxygen Reduction Reaction at LaxCa1-XMnO3 Nanostructures: Interplay between A-Site Segregation and B-Site Valency. *Catal. Sci. Technol.* **2016**, *6* (19), 7231–7238. https://doi.org/10.1039/c6cy01105e.

(30) Poux, T.; Napolskiy, F. S.; Dintzer, T.; Kéranguéven, G.; Istomin, S. Y.; Tsirlina, G. A.; Antipov, E. V.; Savinova, E. R. Dual Role of Carbon in the Catalytic Layers of Perovskite/Carbon Composites for the Electrocatalytic Oxygen Reduction Reaction. *Catal. Today* **2012**, *189* (1), 83–92. https://doi.org/10.1016/j.cattod.2012.04.046.

(31) Yang, C.; Fontaine, O.; Tarascon, J.-M.; Grimaud, A. Chemical Recognition of Active Oxygen Species on the Surface of Oxygen Evolution Reaction Electrocatalysts. *Angew. Chemie Int. Ed.* **2017**, *56* (30), 8652–8656. https://doi.org/10.1002/anie.201701984.

(32) Yang, C.; Laberty-Robert, C.; Batuk, D.; Cibin, G.; Chadwick, A. V.; Pimenta, V.; Yin, W.; Zhang, L.; Tarascon, J.-M.; Grimaud, A. Phosphate Ion Functionalization of Perovskite Surfaces for Enhanced Oxygen Evolution Reaction. *J. Phys. Chem. Lett.* **2017**, *8* (15), 3466–3472. https://doi.org/10.1021/acs.jpclett.7b01504.

(33) Gonell, F.; Alem, N.; Dunne, P.; Crochet, G.; Beaunier, P.; Méthivier, C.; Montero, D.; Laberty-Robert, C.; Doudin, B.; Portehault, D. Versatile Molten Salt Synthesis of Manganite Perovskite Oxide Nanocrystals and Their Magnetic Properties. *ChemNanoMat* **2019**, *5* (3), 358–363. https://doi.org/10.1002/cnma.201800632.

(34) Coey, J. M. D.; Viret, M.; von Molnár, S. Mixed-Valence Manganites. *Adv. Phys.* **1999**, *48* (2), 167–293. https://doi.org/10.1080/000187399243455.

(35) Portehault, D.; Cassaignon, S.; Baudrin, E.; Jolivet, J.-P. Morphology Control of Cryptomelane Type MnO 2 Nanowires by Soft Chemistry. Growth Mechanisms in Aqueous Medium. *Chem. Mater.* **2007**, *19* (22), 5410–5417. https://doi.org/10.1021/cm071654a.

(36) Sánchez-Sánchez, C. M.; Bard, A. J. Hydrogen Peroxide Production in the Oxygen Reduction Reaction at Different Electrocatalysts as Quantified by Scanning Electrochemical Microscopy. *Anal. Chem.* **2009**, *81* (19), 8094–8100. https://doi.org/10.1021/ac901291v.

(37) Villanueva-Rodríguez, M.; Sánchez-Sánchez, C. M.; Montiel, V.; Brillas, E.; Peralta-Hernández, J. M.; Hernández-Ramírez, A. Characterization of Ferrate Ion Electrogeneration in Acidic Media by Voltammetry and Scanning Electrochemical Microscopy. Assessment of Its Reactivity on 2,4-Dichlorophenoxyacetic Acid Degradation. *Electrochim. Acta* **2012**, *64*, 196–204. https://doi.org/10.1016/j.electacta.2012.01.021.

(38) Hsu, H.-Y.; Ji, L.; Du, M.; Zhao, J.; Yu, E. T.; Bard, A. J. Optimization of PbI2 /MAPbI3 Perovskite Composites by Scanning Electrochemical Microscopy. *J. Phys. Chem. C* **2016**, *120* (35), 19890–19895. https://doi.org/10.1021/acs.jpcc.6b07850.

(39) Bard, A. J.; Mirkin, M. V. *Scanning Electrochemical Microscopy*; Marcel Dekker: New York, 2001.

Oxygen reduction electrocatalysts from molten salts